scientific reports

Check for updates

OPEN

Fabrication of hollow flower-like magnetic Fe_3O_4/C/MnO_2/C_3N_4 composite with enhanced photocatalytic activity

Mingliang Ma[1], Yuying Yang[1,3], Yan Chen[1], Jiabin Jiang[1], Yong Ma[2]✉, Zunfa Wang[1], Weibo Huang[1], Shasha Wang[4], Mingqing Liu[1], Dongxue Ma[1] & Xiaoning Yan[1]

The serious problems of environmental pollution and energy shortage have pushed the green economy photocatalysis technology to the forefront of research. Therefore, the development of an efficient and environmentally friendly photocatalyst has become a hotpot. In this work, magnetic Fe_3O_4/C/MnO_2/C_3N_4 composite as photocatalyst was synthesized by combining in situ coating with low-temperature reassembling of CN precursors. Morphology and structure characterization showed that the composite photocatalyst has a hollow core–shell flower-like structure. In the composite, the magnetic Fe_3O_4 core was convenient for magnetic separation and recovery. The introduction of conductive C layer could avoid recombining photo-generated electrons and holes effectively. Ultra-thin g-C_3N_4 layer could fully contact with coupled semiconductor. A Z-type heterojunction between g-C_3N_4 and flower-like MnO_2 was constructed to improve photocatalytic performance. Under the simulated visible light, 15 wt% photocatalyst exhibited 94.11% degradation efficiency in 140 min for degrading methyl orange and good recyclability in the cycle experiment.

In recent years, with the increase of wastewater discharge, a large amount of toxic and harmful organic pollutants are put into the water, which are difficult to completely degrade[1–6]. Advanced photocatalytic oxidation technology with strong oxidation capacity and high efficiency was considered as a very promising wastewater treatment means for the degradation of organic pollutants[7–14]. Among them, semiconductor-based photocatalysts with mild reaction conditions were most widely used[15–22]. In addition, various styles of self-assembled photocatalyst nanostructures were synthesized, such as one-dimensional nanotubes[23], two-dimensional layered structure[24,25], three-dimensional network structure[26], three-dimensional flower-like structure[27] and etc.

MnO_2 has some advantages including low cost, high stability and environmental friendliness. Besieds, its narrow band gap can increase the utilization of visible light, which is very promising as a photocatalyst[28–32]. The layered structure of δ-MnO_2 is formed by the MnO_6 octahedral layer with shared edges, and there are some cations and H_2O molecules between the layers to maintain the charge balance[33]. δ-MnO_2 has been widely used as a catalyst to purify the environment[34–36]. However, while the narrow band gap increases the usage of visible light, it is also accompanied by the rapid recombination of photo-generated electrons and holes. The low photocatalytic efficiency restricts pure MnO_2 for practical applications[37–39].

Coupling MnO_2 with other semiconductors to build a heterojunction is an effective method to prevent the recombination of photo-generated carriers. Wang et al.[40] first reported that g-C_3N_4 could decompose water to generate hydrogen by visible light irradiation. Subsequently, owing to excellent visible light activity and chemical stability, g-C_3N_4 as photocatalyst has attracted a lot of attention[41–43]. Recently, Zhu et al.[44] coated g-C_3N_4 on the semiconductor surface to form an ultra-thin g-C_3N_4 layer, avoiding the low contact rate between the bulk g-C_3N_4 and the coupling semiconductor interface. Therefore, the design of the composite with ultra-thin g-C_3N_4 layer and MnO_2 is expected to achieve significant charge transfer at their interface by facilitating the separation of photo-generated carriers, thereby enhancing photocatalytic activity.

[1]School of Civil Engineering, Qingdao University of Technology, Qingdao 266033, People's Republic of China. [2]School of Material Science and Engineering, Shandong University of Science and Technology, Qingdao 266590, People's Republic of China. [3]Key Laboratory of Marine Environmental Corrosion and Bio-Fouling, Institute of Oceanology, Chinese Academy of Sciences, Qingdao 266071, People's Republic of China. [4]School of Environmental and Municipal Engineering, Qingdao University of Technology, Qingdao 266033, People's Republic of China. ✉email: courage2010@126.com

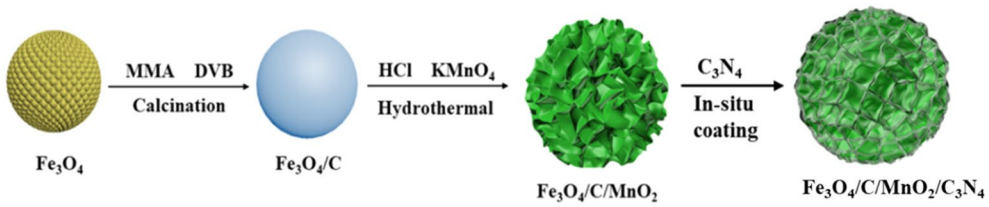

Figure 1. Fabrication of magnetic flower-like $Fe_3O_4/C/MnO_2/C_3N_4$ photocatalyst.

In our previous research, Fe_3O_4 was introduced as a magnetic core to construct a magnetically recyclable core–shell structure photocatalyst. The existence of magnetic core was beneficial to the recycle of the catalyst[45,46]. In this paper, hollow Fe_3O_4 microspheres were also synthesized by using a hydrothermal method as magnetic cores. Subsequently, the carbon layer was obtained by calcining the polymer layer formed on the periphery of Fe_3O_4 microspheres, which can protect the core and act as an electronic conductor simultaneously. Then, flower-like MnO_2 was grown on the periphery of Fe_3O_4/C microspheres through the hydrothermal method. Finally, the transparent CN precursor produced with the aid of the neutral hydrothermal process was polymerized in situ on the surface of above microspheres at a low temperature. A flower-like $Fe_3O_4/C/MnO_2/C_3N_4$ composite photocatalyst with core–shell structure was obtained. The photocatalyst displayed remarkable photocatalytic activity for degrading the organic dye methyl orange (MO). The specific synthetic steps are shown in Fig. 1.

Experimental section

Preparation of Fe_3O_4/C core–shell composite. First, hollow Fe_3O_4 microspheres were obtained by the hydrothermal method[47]. Then the polymer layer was prepared through a distillation precipitation process. 0.10 g Fe_3O_4 microspheres were ultrasonically dispersed in 80 mL acetonitrile. 1.0 mL divinylbenzene (DVB), 1.0 mL methyl methacrylate (MMA), and 0.040 g 2,2-azobisisobutyronitrile (AIBN) were also added into the above solution. The system was heated in 90 °C water bath for 2 h. Afterwards, Fe_3O_4/P(MMA-DVB) microspheres were obtained by using an external magnet, and washed three times. Then, the Fe_3O_4/P(MMA-DVB) sample was calcined at 600 °C for 2.0 h to obtain Fe_3O_4/C microspheres.

Preparation of $Fe_3O_4/C/MnO_2$ flower-like composite. 0.30 g Fe_3O_4/C microspheres were fully dispersed to 80 mL 0.055 M $KMnO_4$ solution. Next, 1.0 mL HCl was added to the mixture dropwise. Thereafter, the mixture was transferred to an autoclave and heated to 100 °C for 6.0 h. At last, flower-like $Fe_3O_4/C/MnO_2$ microspheres with core–shell structure were obtained by using an external magnet, and washed three times and lyophilized.

Preparation of $Fe_3O_4/C/MnO_2/C_3N_4$ composite. 6.0 g dicyandiamide was calcined at 550 °C for 4.0 h to produce g-C_3N_4. Thereafter, 2.0 g g-C_3N_4 powder was dispersed in 80 mL deionized water, and then heated at 210 °C for 6 h to form a CN transparent precursor. $Fe_3O_4/C/MnO_2$ microspheres were added to the precursor (5.0, 10, 15, 20, 30 wt%). The solvent was slowly removed through a lyophilized process. Finally, $Fe_3O_4/C/MnO_2/C_3N_4$ flower-like photocatalyst was obtained via annealing at 200 °C for 4.0 h in a tube furnace under N_2 protection.

Characterization. Scanning electron microscope (SEM, JSM-6700F, JEOL Ltd., Japan) was employed to obtain a surface topography image of the samples. Transmission images were gotten by using a high-resolution transmission electron microscope (TEM, JEM-3010, Hitachi Co., Japan). X-ray diffraction patterns of samples were obtained by the use of an X-ray diffractometer (XRD, Shimadzu XRD-7000, Shimadzu Co., Japan). X-ray photoelectron spectrometer (XPS, JPS-9010 MC, JEOL Ltd., Japan) was utilized to obtain the samples' surface elemental composition of the samples. Brunauer–Emmett–Teller (BET, ASAP 2020, Quantachrome, US) means was used to test the pore size and specific surface area of the catalyst. The saturation magnetization of the samples was obtained by employing a vibrating sample magnetometer (VSM, Lake Shore 7307, Lake Shore Ltd., USA). A photochemical reactor (BL-GHX-V, Shanghai Bilang Instruments Co., Ltd., China) was used to simulate the illumination. The ultraviolet–visible absorption spectra were measured on an ultraviolet–visible spectrophotometer (UV–vis, UV-5200PC, YuanXi, China).

Photocatalytic experiment. Firstly, 20 mg $Fe_3O_4/C/MnO_2/C_3N_4$ photocatalyst were added to 65 mL, 10 mg/L MO solution. Under dark environment, the mixture was agitated to reach adsorbed-desorbed equilibrium. Secondly, photocatalytic reaction was carried out with simulate light stemming from a 400 W metal halide lamp. The absorbance of the solution at intervals was monitored with the help of UV–visible spectrophotometer. Ultimately, the degradation curves of the MO solution were recorded, followed by the calculation of photocatalytic degradation rate.

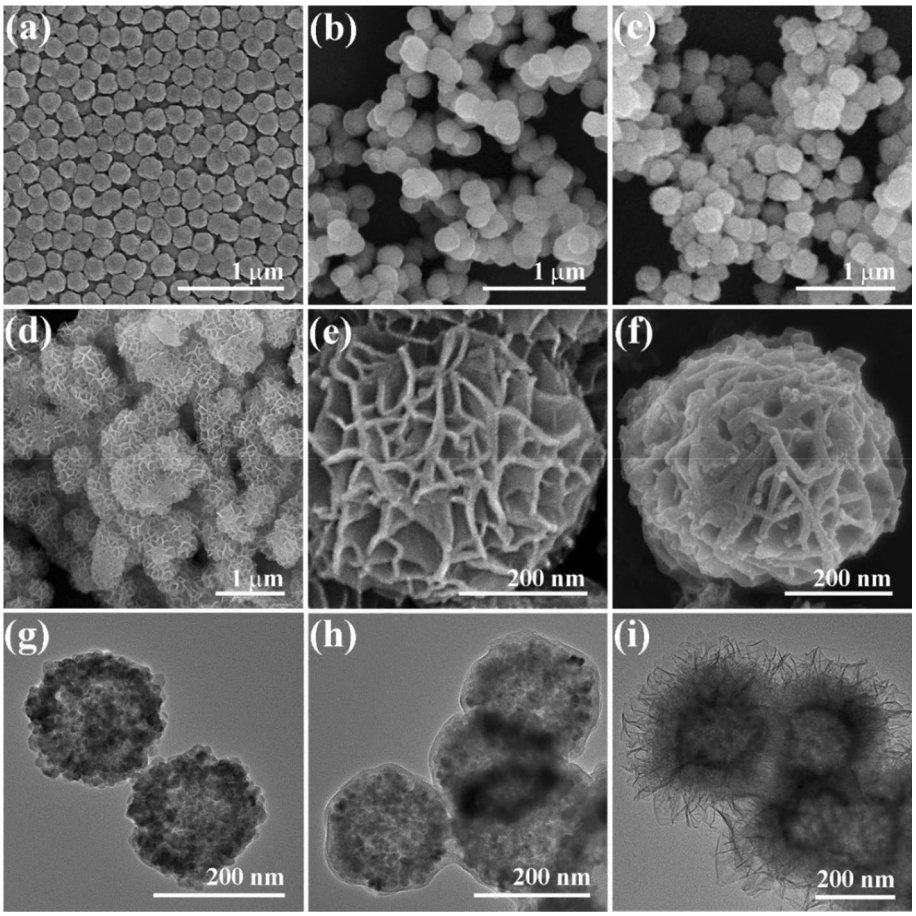

Figure 2. SEM images of hollow Fe_3O_4 microspheres (**a**), Fe_3O_4/P(MMA-DVB) microspheres (**b**), Fe_3O_4/C microspheres (**c**), Fe_3O_4/C/MnO_2 flower-like microspheres (**d**,**e**), and Fe_3O_4/C/MnO_2/C_3N_4 flower-like microspheres (**f**), TEM images of hollow Fe_3O_4 microspheres (**g**), Fe_3O_4/C core–shell microspheres (**h**) and flower-like Fe_3O_4/C/MnO_2/C_3N_4 microspheres (**i**).

Results and discussion

SEM and TEM images of samples are shown in Fig. 2. In Fig. 2a, Fe_3O_4 microspheres prepared by the hydrothermal method have good dispersibility and uniform size of about 200 nm. Figure 2b shows Fe_3O_4/P(MMA-DVB) microspheres prepared by distillation precipitation process. Compared with the former, the surface of the latter becomes much smoother, which proves the successful formation of polymer coating. And these polymer core–shell microspheres have a diameter of 225 nm. To obtain the conductive carbon layer, the polymer microspheres were calcined and carbonized. The SEM image of Fe_3O_4/C microspheres is displayed in Fig. 2c. One can see that the original core–shell structure of the material is not destroyed after the calcination treatment. And the agglomeration that originally occurred in Fe_3O_4/P(MMA-DVB) polymer microspheres has been slightly weakened due to the carbonization treatment. From Fig. 2d,e, it can be found out that the flower-like morphology of the composite microspheres produced by the hydrothermal method is composed of MnO_2 intersecting sheets. And the overall particle size is about 480 nm. As shown in Fig. 2f, the overall flower-like morphology has not changed, but the thickness of the MnO_2 flower sheets has increased significantly. This case indicates that the ultra-thin C_3N_4 layer is successfully formed on the surface of MnO_2 to form a flower-like Fe_3O_4/C/MnO_2/C_3N_4 composite photocatalyst. It can be seen from Fig. 2g that the synthesized magnetic microspheres have a clear hollow structure with a particle size of about 200 nm. Figure 2h shows the TEM image of the Fe_3O_4/C microspheres, which have a core–shell structure with 13 nm thickness of C shell. Figure 2i is the TEM image of the flower-like Fe_3O_4/C/MnO_2/C_3N_4 microspheres. It can be found out that the composite photocatalyst with a complete magnetic core and flower-like shell exhibits the diameter of around 480 nm. According to these results, the composite photocatalyst with a magnetic core and flower-like shell was successfully prepared.

The crystal phase composition of the composite was demonstrated by XRD characterization, as shown in Fig. 3I. Figure 3I-a is the diffraction curve of the bulk g-C_3N_4 obtained by pyrolysis of dicyandiamide. The strong peak near 27.4° belongs to the (002) plane, corresponding to the crystal plane stack of the CN aromatic system[48]. The broad peak at 13.0° belongs to the (100) plane ascribed to the triazine repeat unit[44]. Figure 3I-b is the diffraction curve of Fe_3O_4 microspheres showing the diffraction peaks at 30.12°, 35.41°, 43.10°, 53.43°, 57.11°, and 62.52°, which are attributed to (220), (311), (400), (422), (511) and (440) crystal planes of Fe_3O_4 (JCDPS

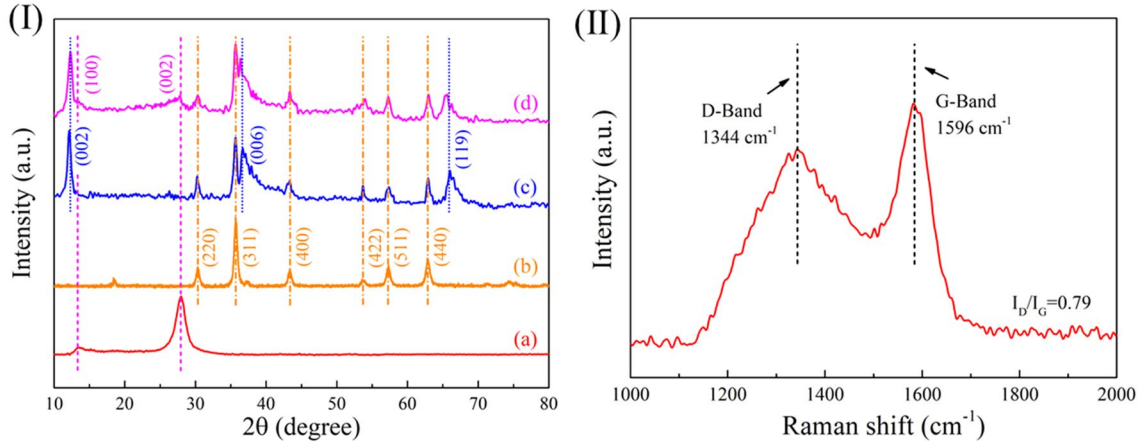

Figure 3. (**I**) XRD patterns of pure g-C_3N_4 (**a**), Fe_3O_4 microspheres (**b**), Fe_3O_4/C/MnO_2 flower-like microspheres (**c**) and Fe_3O_4/C/MnO_2/C_3N_4 flower-like microspheres (**d**). (**II**): Raman spectrum of Fe_3O_4/C microspheres.

85-1436)[49]. The sharp peaks indicate that the synthesized Fe_3O_4 are well crystallized. In Fig. 3I-c, in addition to the diffraction peaks of Fe_3O_4 component, the diffraction peaks at 12.20°, 36.70°, and 65.70° correspond to (002), (006), and (119) crystal planes, in consistence with the crystal planes of MnO_2 (JCDPS 18-0802)[50]. This case indicates that the MnO_2 is successfully synthesized. The diffraction curve of the Fe_3O_4/C/MnO_2/C_3N_4 photocatalyst in Fig. 3I-d reveals that except for the diffraction peaks of Fe_3O_4 and MnO_2, the diffraction peaks appear at 13.00° and 27.40° are separately assigned to the (100) and (002) crystal planes of g-C_3N_4. This situation indicates that CN precursor successfully becomes g-C_3N_4 after low temperature polymerization and high temperature calcination. XRD results show that the Fe_3O_4/C/MnO_2/C_3N_4 composite photocatalyst were successfully synthesized.

The XRD patterns cannot verify the existence of the C layer. For further confirming the formation of the C layer, the Raman test was used to characterize the Fe_3O_4/C sample. The spectrum in Fig. 3II indicates two different peaks at 1344 cm^{-1} and 1596 cm^{-1}, corresponding to D-band and G-band of carbon material, respectively. These results confirm the carbonization of Fe_3O_4/P(MMA-DVB) material, and Fe_3O_4/C microspheres are successfully obtained. These two bands are related to the A_{1g} phonon of sp^3 carbon atoms in disordered graphite and the in-plane vibration of sp^2 carbon atoms in the crystalline graphite, respectively[51]. The peak intensity ratio (I_D/I_G) can evaluate the carbon material's crystallinity. The smaller the value is, the higher the degree of atomic order is[52]. Herein, the value is 0.79, meaning that the carbon material is graphitized partially. Therefore, the presence of the carbon matrix can improve the electronic conductivity and help avoid the recombination of photo-generated electron holes.

The surface chemical composition and the chemical state of the products were demonstrated by XPS characterization. Figure 4a is the full-scan spectrum of the photocatalyst, presenting the peaks of Mn, O, N, and C elements. From Fig. 4b, as for the Mn 2*p* spectrum, two peaks at 653.9 eV and 642.3 eV correspond to Mn $2p_{1/2}$ and Mn $2p_{3/2}$. With respect to the O1*s*, as illustrated in Fig. 4c, three peaks at 529.7 eV, 531.3 eV, 533.2 eV are fitted, which are separately attributed to the Mn–O–Mn lattice oxygen, surface hydroxyl and surface adsorbed oxygen. The C1*s* spectrum in Fig. 4d shows the sub-bands centered at 284.8 eV and 288.5 eV, which are ascribed to the C–C coordination of the surface-unstable carbon and N=C–N_2 of g-C_3N_4. In addition, there is another peak centering at 286.3 eV, which is assigned to the C-O bond formed between the C of C_3N_4 and the O of MnO_2. This result indicates that MnO_2 and g-C_3N_4 are closely connected and form a solid MnO_2/g-C_3N_4 interface, promoting the transfer and separation of photo-generated carriers. In the case of the N1*s* spectrum (Fig. 4e), the peaks at 399.4 eV, 400.5 eV, 401.8 eV, and 405.3 eV are separately designated as carbon-bonded sp^2 hybrid aromatic C=N–C, a tertiary nitrogen bonded to a carbon atom in the form N–$(C)_3$, NH and the charge effect or positive charge localization in the heterocyclic ring. The XPS spectra powerfully verify the surface chemical composition of the Fe_3O_4/C/MnO_2/C_3N_4 photocatalyst.

The specific surface area and the pore structure of Fe_3O_4, Fe_3O_4/C, Fe_3O_4/C/MnO_2 and Fe_3O_4/C/MnO_2/C_3N_4 products are listed in Table 1. The former of the Fe_3O_4/C/MnO_2 and Fe_3O_4/C/MnO_2/C_3N_4 products are 119.56 m^2/g and 120.25 m^2/g, and the latter of them are 0.35 cm^3/g and 0.31 cm^3/g. Since C_3N_4 does not significantly affect the morphology of the composite structure, these parameters of the two samples are almost similar. The higher values are owing to the flower-like structure of the composite photocatalyst. The increase in specific surface area is conducive to exposing more active sites and increasing more surface adsorption, followed by improving catalytic performance.

To evaluate the saturation magnetization value of Fe_3O_4, Fe_3O_4/C, Fe_3O_4/C/MnO_2 and Fe_3O_4/C/MnO_2/C_3N_4, VSM measurement is conducted. It can be seen from Fig. 5a that the magnetization value of the Fe_3O_4 microspheres is 70.58 emu/g. After the carbon layer is recombined, the value of Fe_3O_4/C microspheres decreases to 56.97 emu/g (Fig. 5b). After the flower-like MnO_2 was fabricated, the content of Fe_3O_4 component is decreasing, which leads to the value of Fe_3O_4/C/MnO_2 microspheres decreases obviously to 37.62 emu/g (Fig. 5c). With the further formation of g-C_3N_4, the value is 30.02 emu/g (Fig. 5d). This value still meets the needs of magnetic separation. As shown in the illustration, when the magnet is placed next to the Fe_3O_4/C/MnO_2/C_3N_4 photocatalyst

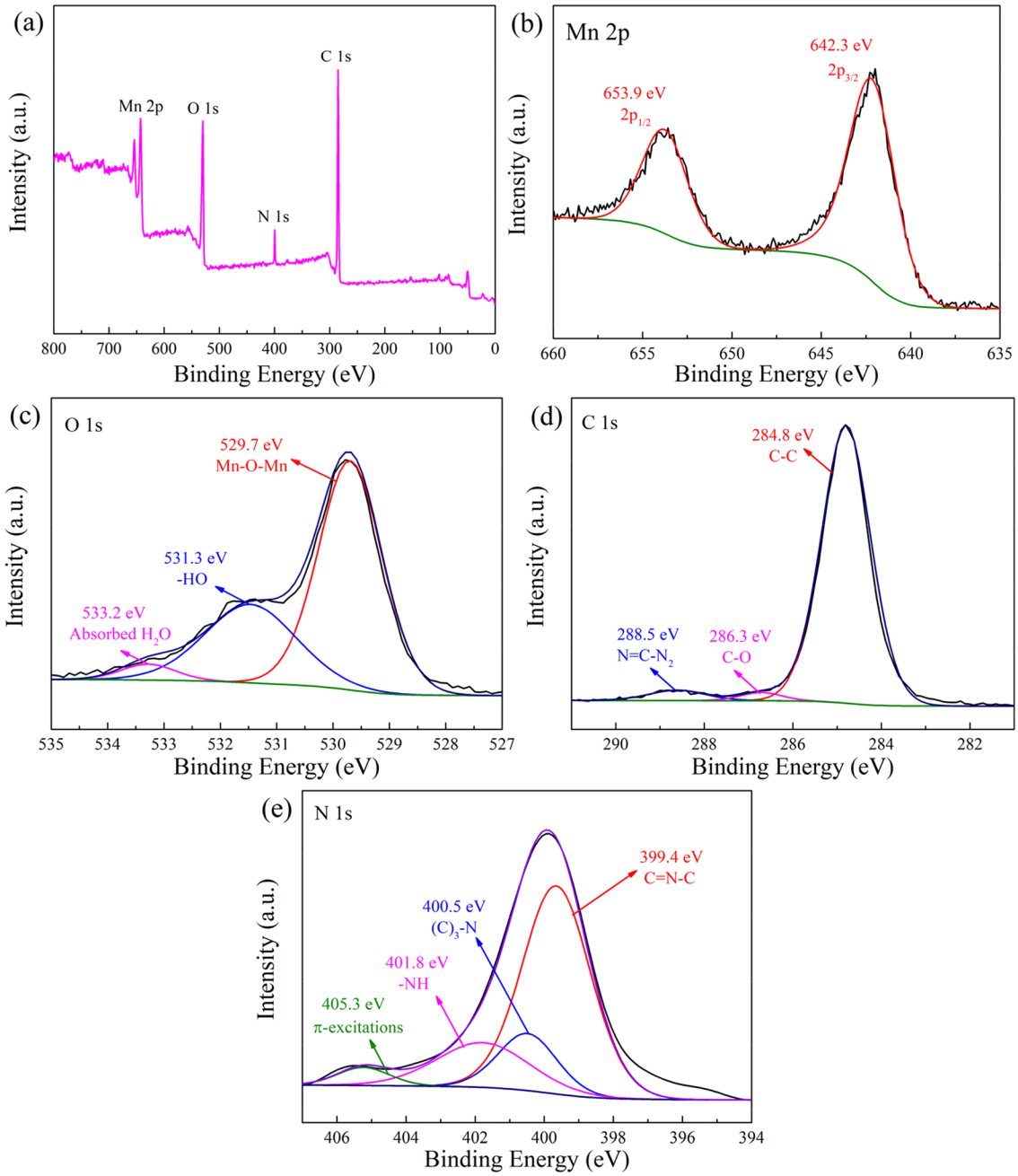

Figure 4. XPS spectra of $Fe_3O_4/C/MnO_2/C_3N_4$ photocatalyst (**a**), Mn 2*p* (**b**), O1*s* (**c**), C1*s* (**d**) and N1*s* (**e**).

Entry	Sample	Surface area (m^2/g)	Pore width (nm)	Pore volume (cm^3/g)
1	Fe_3O_4	38.47	4.01	0.17
2	Fe_3O_4/C	59.87	2.23	0.21
3	$Fe_3O_4/C/MnO_2$	119.56	6.94	0.35
4	$Fe_3O_4/C/MnO_2/C_3N_4$	120.25	6.35	0.31

Table 1. Specific surface area and pore parameters of samples.

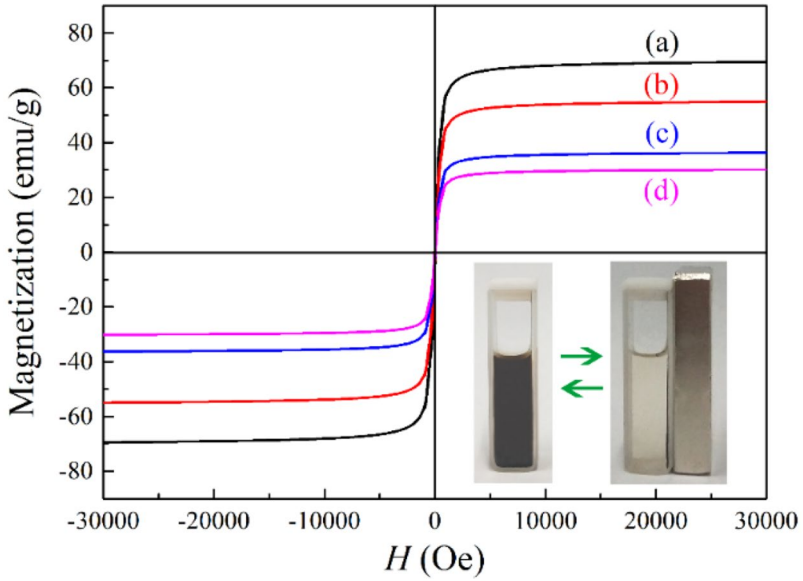

Figure 5. Hysteresis loop spectra of Fe_3O_4 microspheres (**a**), Fe_3O_4/C core–shell microspheres (**b**), Fe_3O_4/C/MnO_2 flower-like microspheres (**c**) and flower-like Fe_3O_4/C/MnO_2/C_3N_4 photocatalyst (**d**).

suspension, the photocatalyst can be quickly attracted to the side of the cuvette in a short time. The results show that the photocatalyst has a good magnetic response to the magnetic field, favoring the magnetic separation from the mixed solution.

Determining the adsorption capacity of the photocatalyst in dark reaction, then degrading MO under simulated light is used to investigate the photocatalytic activity of the prepared photocatalyst, and the results are shown in Fig. 6. Figure 6a reveals the mixture reached adsorption–desorption equilibrium within 60 min. And Fe_3O_4/C/MnO_2/C_3N_4 can adsorb about 22% of MO within 60 min, which is related to its higher specific surface area (120.25 m^2/g). Figure 6b displays that UV–Vis is employed to monitor the change in the absorbance of the solution during the photocatalytic reaction. In Fig. 6b, one can clearly view that MO was almost completely degraded with adding Fe_3O_4/C/MnO_2/C_3N_4 composite photocatalyst after 140 min. The photocatalytic degradation MO over Fe_3O_4/C/MnO_2/C_3N_4 could be described by the following reactions:

$$\text{photocatalyst} + h\nu \rightarrow \text{photocatalyst}\left(e^-\right) + \text{photocatalyst}\left(h^+\right) \quad (1)$$

$$H_2O + h^+ \rightarrow {}^{\cdot}OH + H^+ \quad (2)$$

$$O_2 + e^- \rightarrow {}^{\cdot}O_2^- \quad (3)$$

$$MO + {}^{\cdot}OH/O_2^- \rightarrow \text{Mineralisation products} \quad (4)$$

Figure 6c indicates the change of the MO concentration ratio C_t/C_0 with varying the light time, in which C_0 and C_t are the initial concentration of MO and the concentration of MO during the reaction, respectively. The degradation rate of MO solution with Fe_3O_4/C/MnO_2/C_3N_4 photocatalyst reaches 94.11%. From Fig. 6d, this reaction is attributed to a pseudo first-order reaction, which belongs to the Langmuir–Hinshelwood model with $\ln(C_t/C_0) = -kt$. In the formula, k is the apparent first-order rate constant. The calculated rate constant k of Fe_3O_4/C/MnO_2/C_3N_4 photocatalyst is 0.022 min^{-1}. The excellent photocatalytic performance of Fe_3O_4/C/MnO_2/C_3N_4 composite material benefits from the synergistic effect between the various components.

In order to find the optimal ratio, the effect of amount of g-C_3N_4 on the photocatalytic efficiency was investigated. Meanwhile, determining the minimum optimal amount of photocatalyst in practical applications is important to reduce the costs. The composite photocatalyst containing different amounts of g-C_3N_4 (5%, 10%, 15%, 20%, 30%) were used to degrade MO dyes under the same conditions. From Fig. 7a,b, when the amount of g-C_3N_4 is 15%, the Fe_3O_4/C/MnO_2/C_3N_4 composite photocatalyst has the highest value. In Fig. 7c, the effect of the amount of photocatalyst on the degradation efficiency is examined. The results show that the photocatalytic efficiency gradually increases when the amount of photocatalyst increases in the range of 0–20 mg, due to the effective reaction area and the reactive site increase. When the amount of photocatalyst continues to increase, the photocatalytic efficiency does not change significantly, which may be caused by the particle agglomeration affecting the increase of active sites. Therefore, the optimal dosage of Fe_3O_4/C/MnO_2/C_3N_4 photocatalyst is 20 mg. Considering the industrial application of Fe_3O_4/C/MnO_2/C_3N_4 nanoparticles, it is essential to investigate the recyclability and stability of the photocatalyst. The Fe_3O_4/C/MnO_2/C_3N_4 was reused four times to examine their

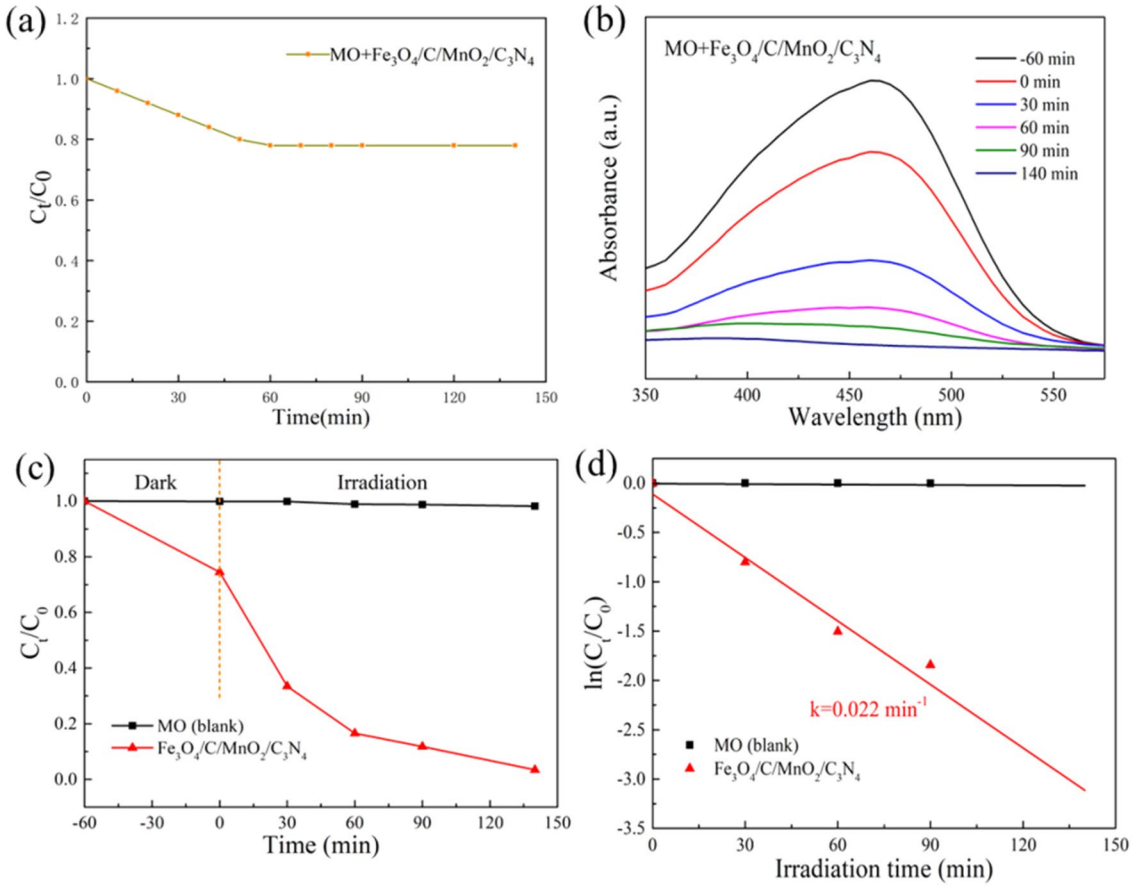

Figure 6. Adsorption of MO on sample in dark reaction (**a**), UV–vis spectra of MO solution at different times in the presence of $Fe_3O_4/C/MnO_2/C_3N_4$ photocatalyst (**b**), C_t/C_0 change with time (**c**), first-order kinetic model linear fit (**d**). Reaction conditions: [MO] = 65 mL, 10 mg/L, [photocatalyst] = 20 mg, [light] = 400 W metal halide lamp, T = 25 °C, t = 140 min.

performances. And Fig. 7d reveals the results that the degradation rates for the four cycles are 94.11%, 90.42%, 88.37% and 79.69%, respectively. There is no doubt that after the photocatalyst is recycled, the conversion rate will decrease, which might result from the loss of sample during the cycle. However, even after four cycles, the value still has 79.69% that might be related with the structure stability of the used photocatalysts, strongly demonstrating that the designed photocatalyst has excellent recyclability.

In this study, $Fe_3O_4/C/MnO_2/C_3N_4$ photocatalyst was synthesized by compounding g-C_3N_4 on the surface of MnO_2. In terms of enhanced photocatalytic activity, it is assumed that the charge transfer in the photocatalyst uses the Z-type mechanism, as shown in Fig. 8. For the individual g-C_3N_4 or MnO_2 component, due to thermodynamic effects, photo-generated holes in g-C_3N_4 cannot oxidize OH^- to form •OH radicals, while photo-generated electrons in MnO_2 cannot generate $^{\cdot}O_2^-$ radicals effectively. Therefore, individual g-C_3N_4 or MnO_2 material cannot possess good photocatalytic performances. However, after a heterojunction was fabricated between these two components, the photo-generated electrons in the conduction band of MnO_2 can be transferred to the valence band of g-C_3N_4 and combined with the photo-generated holes there. This configuration of the Z-type scheme makes the utilization of holes from MnO_2 and electrons from g-C_3N_4 remarkably enhanced. In addition, the conductive C layer can also increase the photo-generated electron–hole pairs' separation in MnO_2, which effectively prevents the recombination of photo-generated carriers. In the meantime, the higher specific surface area supplies much more active sites for photocatalytic activities. The prepared flower-like $Fe_3O_4/C/MnO_2/C_3N_4$ photocatalyst forms a Z-type photocatalytic system, which effectively enhances the separation of carrier, so that the composite material has excellent photocatalytic degradation efficiency.

Conclusions

In summary, a magnetic recyclable flower-like $Fe_3O_4/C/MnO_2/C_3N_4$ heterojunction photocatalyst was prepared for degrading organic dyes. The Fe_3O_4 core was used to facilitate magnetic separation and recovery. The C layer could conduct photo-generated electrons in MnO_2 and protect the core. The thin g-C_3N_4 layer was compounded on the surface of MnO_2, which greatly improved the specific surface area and the reactive sites of the material. The obtained $Fe_3O_4/C/MnO_2/C_3N_4$ composites exhibited enhanced photocatalytic performance for the degradation of MO solution (65 mL, 10 mg/L) under simulated light irradiation. The maximum photocatalytic degradation efficiency was 94.11% within 140 min. It was assumed that a Z-type heterojunction was fabricated between

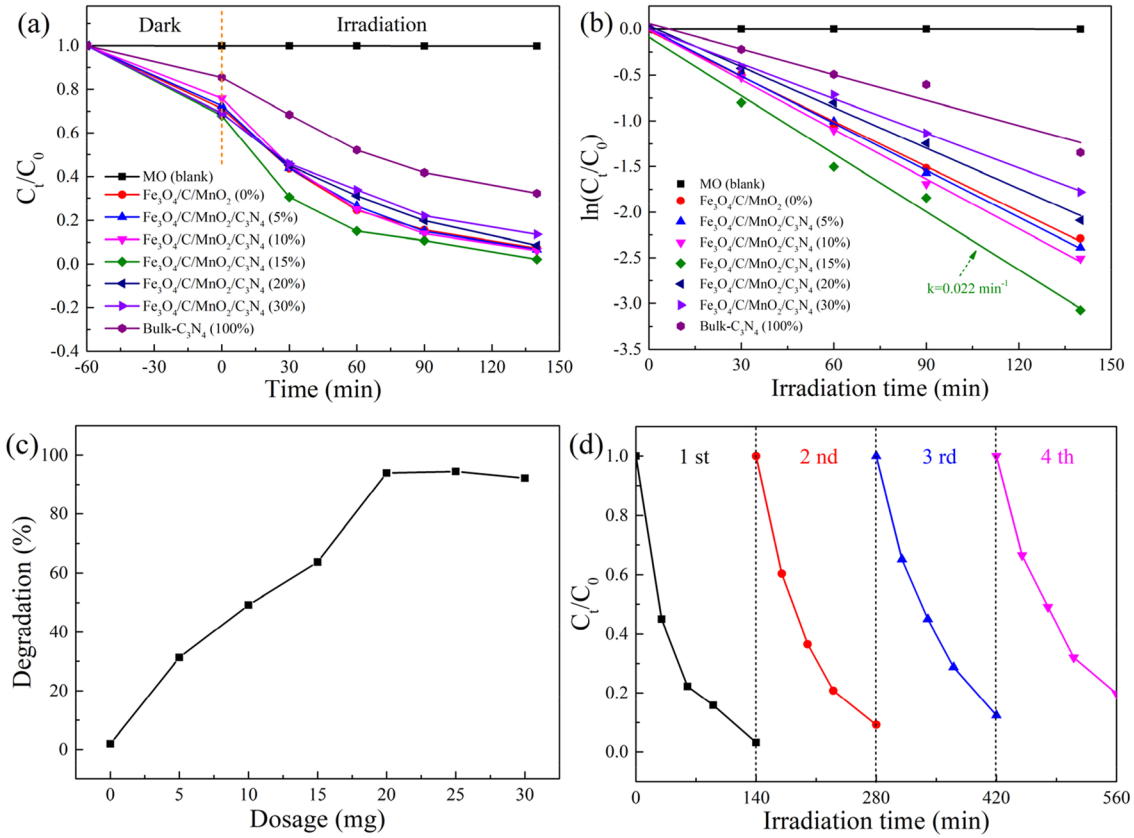

Figure 7. Effect of the amount of C_3N_4 on the degradation of MO (**a**,**b**), effect of the amount of $Fe_3O_4/C/MnO_2/C_3N_4$ photocatalyst on the degradation of MO (**c**), cyclic test of MO degradation of $Fe_3O_4/C/MnO_2/C_3N_4$ photocatalyst (**d**). Reaction conditions: [MO] = 65 mL, 10 mg/L, [light] = 400 W metal halide lamp, T = 25 °C, t = 140 min. For (**a**,**b**,**d**), [photocatalyst] = 20 mg.

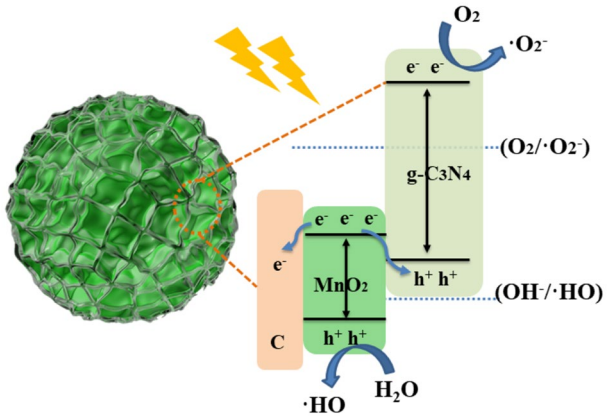

Figure 8. Schematic diagram of possible mechanism of $Fe_3O_4/C/MnO_2/C_3N_4$ photocatalyst.

MnO_2 and g-C_3N_4, which stimulated the electron transfer from the valence band of MnO_2 to the conduction band of g-C_3N_4. This structure promoted the photo-generated electron–hole pairs' separation, inhibited the free charges' recombination, and improved effective use of visible light. In here, an effective method to construct heterostructure nanomaterials was provided for efficient photocatalytic degradation.

Received: 22 November 2020; Accepted: 14 January 2021
Published online: 28 January 2021

References

1. Masuda, Y. Bio-inspired mineralization of nanostructured TiO_2 on PET and FTO films with high surface area and high photocatalytic activity. *Sci. Rep.* **10**, 13499 (2020).
2. Lee, M. Y. *et al.* Comparison of UV/H_2O_2 and UV/PS processes for the treatment of reverse osmosis concentrate from municipal wastewater reclamation. *Chem. Eng. J.* **388**, 124260 (2020).
3. Liu, N. *et al.* Magnetic Fe_3O_4@MIL-53(Fe) nanocomposites derived from MIL-53(Fe) for the photocatalytic degradation of ibuprofen under visible light irradiation. *Mater. Res. Bull.* **132**, 111000 (2020).
4. Takanabe, K. Photocatalyticwater splitting: quantitative approaches toward photocatalyst by design. *ACS Catal.* **7**, 8006–8022 (2017).
5. Kumar, M., Basera, P., Saini, S. & Bhattacharya, S. Theoretical insights of codoping to modulate electronic structure of TiO_2 and $SrTiO_3$ for enhanced photocatalytic efficiency. *Sci. Rep.* **10**, 15372 (2020).
6. Fu, J., Xu, Q., Low, J., Jiang, C. & Yu, J. Ultrathin 2D/2D WO_3/g-C_3N_4 step-scheme H_2 production photocatalyst. *Appl. Catal. B Environ.* **243**, 556–565 (2019).
7. Trojanowicz, M., Bojanowska-Czajka, A., Bartosiewicz, I. & Kulisa, K. Advanced oxidation/reduction processes treatment for aqueous perfluorooctanoate (PFOA) and perfluorooctanesulfonate (PFOS): a review of recent advances. *Chem. Eng. J.* **336**, 170–199 (2018).
8. Hodges, B. C., Cates, E. L. & Kim, J.-H. Challenges and prospects of advanced oxidation water treatment processes using catalytic nanomaterials. *Nat. Nanotechnol.* **13**, 642–650 (2018).
9. Xu, J., Olvera-Vargas, H., Loh, B. J. H. & Lefebvre, O. FTO-TiO_2 photoelectrocatalytic degradation of triphenyltin chloride coupled to photoelectro-Fenton: a mechanistic study. *Appl. Catal. B Environ.* **271**, 118923 (2020).
10. Zhang, G. *et al.* Layered double hydroxides-based photocatalysts and visible-light driven photodegradation of organic pollutants: a review. *Chem. Eng. J.* **392**, 123684 (2020).
11. Sakhare, P. A. *et al.* Magnetically recoverable $BiVO_4$/$NiFe_2O_4$ nanocomposite photocatalyst for efficient detoxification of polluted water under collected sunlight. *Mater. Res. Bull.* **129**, 110908 (2020).
12. Zhang, Z. *et al.* Synthesis of 1D $Bi_{12}O_{17}Cl_xBr_{2-x}$ nanotube solid solutions with rich oxygen vacancies for highly efficient removal of organic pollutants under visible light. *Appl. Catal. B Environ.* **269**, 118774 (2020).
13. Ma, Y. *et al.* Tuning polyaniline nanostructures via end group substitutions and their morphology dependent electrochemical performances. *Polymer* **156**, 128–135 (2018).
14. Ma, Y. *et al.* Morphology-dependent electrochemical supercapacitors in multi-dimensional polyaniline nanostructures. *J. Mater. Chem. A* **5**, 14041–14052 (2017).
15. Ran, J., Jaroniec, M. & Qiao, S. Z. Cocatalysts in semiconductor-based photocatalytic CO_2 reduction: achievements, challenges, and opportunities. *Adv. Mater.* **30**, 1704649 (2018).
16. Liu, D. *et al.* In-situ fabrication of atomic charge transferring path for constructing heterojunction photocatalysts with hierarchical structure. *Appl. Catal. B Environ.* **248**, 459–465 (2019).
17. Jiang, D. *et al.* MoS_2/$SnNb_2O_6$ 2D/2D nanosheet heterojunctions with enhanced interfacial charge separation for boosting photocatalytic hydrogen evolution. *J. Colloid Interface Sci.* **536**, 1–8 (2019).
18. Zhong, J. *et al.* Opposite photocatalytic oxidation behaviors of BiOCl and TiO_2: direct hole transfer vs. indirect (OH)–O-center dot oxidation. *Appl. Catal. B Environ.* **241**, 514–520 (2019).
19. Weng, B., Qi, M.-Y., Han, C., Tang, Z.-R. & Xu, Y.-J. Photocorrosion inhibition of semiconductor-based photocatalysts: basic principle, current development, and future perspective. *Acs Catal.* **9**, 4642–4687 (2019).
20. Wang, F., Li, Q. & Xu, D. Recent progress in semiconductor-based nanocomposite photocatalysts for solar-to-chemical energy conversion. *Adv. Energy Mater.* **7**, 1700529 (2017).
21. Ma, Y. *et al.* Solid polyaniline dendrites consisting of high aspect ratio branches self-assembled using sodium lauryl sulfonate as soft templates: synthesis and electrochemical performance. *Polymer* **182**, 121808 (2019).
22. Ma, Y. *et al.* Three-dimensional core-shell Fe_3O_4/polyaniline coaxial heterogeneous nanonets: preparation and high performance supercapacitor electrodes. *Electrochim. Acta* **315**, 114–123 (2019).
23. Geng, R. *et al.* In situ construction of Ag/TiO_2/g-C_3N_4 heterojunction nanocomposite based on hierarchical co-assembly with sustainable hydrogen evolution. *Nanomaterials* **10**, 1 (2020).
24. Li, K. K. *et al.* Fabrication of tunable hierarchical MXene@AuNPs nanocomposites constructed by self-reduction reactions with enhanced catalytic performances. *Sci. China Mater.* **61**, 728–736 (2018).
25. Yin, J. J. *et al.* Facile preparation of self-assembled MXene@Au@CdS nanocomposite with enhanced photocatalytic hydrogen production activity. *Sci. China Mater.* **63**, 2228–2238 (2020).
26. Jiao, T. F. *et al.* Self-assembly reduced graphene oxide nanosheet hydrogel fabrication by anchorage of chitosan/silver and its potential efficient application toward dye degradation for wastewater treatments. *ACS Sustain. Chem. Eng.* **3**, 3130–3139 (2015).
27. Gao, S. *et al.* A novel 3D hollow magnetic Fe_3O_4/BiOI heterojunction with enhanced photocatalytic performance for bisphenol A degradation. *Chem. Eng. J.* **307**, 1055–1065 (2017).
28. Das, S., Sarnanta, A. & Jana, S. Light-assisted synthesis of hierarchical flower-like MnO_2 nanocomposites with solar light induced enhanced photocatalyticactivity. *ACS Sustain. Chem. Eng.* **5**, 9086–9094 (2017).
29. Wang, H., Chen, S., Wang, Z., Zhou, Y. & Wu, Z. A novel hybrid Bi_2MoO_6 MnO_2 catalysts with the superior plasma induced pseudo photocatalytic-catalytic performance for ethyl acetate degradation. *Appl. Catal. B Environ.* **254**, 339–350 (2019).
30. Liu, Y. *et al.* Promoted oxygen activation of layered micro-mesoporous structured titanium phosphate nanoplates by coupling nano-sized delta-MnO_2 with surface pits for efficient photocatalytic oxidation of CO. *Appl. Catal. B Environ.* **254**, 260–269 (2019).
31. Ding, Y. *et al.* Rational design of Z-scheme PtS-$ZnIn_2S_4$/WO_3-MnO_2 for overall photo catalytic water splitting under visible light. *Appl. Catal. B Environ.* **258**, 117948 (2019).
32. Yang, Y. *et al.* UV–vis-infrared light-driven photothermocatalytic abatement of CO on Cu doped ramsdellite MnO_2 nanosheets enhanced by a photoactivation effect. *Appl. Catal. B Environ.* **224**, 751–760 (2018).
33. Liang, X. *et al.* Coupled morphological and structural evolution of delta-MnO_2 to alpha-MnO_2 through multistage oriented assembly processes: the role of Mn(iii). *Environ. Sci. Nano* **7**, 238–249 (2020).
34. Zhang, Y., Li, H., Zhang, L., Gao, R. & Dai, W.-L. Construction of highly efficient 3D/2D MnO_2/g-C_3N_4 nanocomposite in the epoxidation of styrene with TBHP. *ACS Sustain. Chem. Eng.* **7**, 17008–17019 (2019).
35. Huang, J. *et al.* Effects of MnO_2 of different structures on activation of peroxymonosulfate for bisphenol A degradation under acidic conditions. *Chem. Eng. J.* **370**, 906–915 (2019).
36. Xu, Y. *et al.* Selective conversion of syngas to aromatics over Fe_3O_4@MnO_2 and hollow HZSM-5 bifunctional catalysts. *ACS Catal.* **9**, 5147–5156 (2019).
37. Zhao, J. *et al.* Energy-efficient fabrication of a novel multivalence Mn_3O_4–MnO_2 heterojunction for dye degradation under visible light irradiation. *Appl. Catal. B Environ.* **202**, 509–517 (2017).
38. Chen, M. *et al.* FeOOH-loaded MnO_2 nano-composite: an efficient emergency material for thallium pollution incident. *J. Environ. Manag.* **192**, 31–38 (2017).
39. Zhang, Z. *et al.* Conversion of $CaTi_{1-x}Mn_xO_3$ delta based photocatalyst for photocatalytic reduction of NO via structure-reforming of Ti-bearing blast furnace slag. *ACS Sustain. Chem. Eng.* **7**, 10299–10309 (2019).

40. Wang, X. *et al.* A metal-free polymeric photocatalyst for hydrogen production from water under visible light. *Nat. Mater.* **8**, 76–80 (2009).
41. Lin, L. *et al.* Crystalline carbon nitride semiconductors prepared at different temperatures for photocatalytic hydrogen production. *Appl. Catal. B Environ.* **231**, 234–241 (2018).
42. Fu, J., Yu, J., Jiang, C. & Cheng, B. g-C_3N_4 based heterostructured photocatalysts. *Adv. Energy Mater.* **8**, 1701503 (2018).
43. Yang, C., Wang, B., Zhang, L., Yin, L. & Wang, X. Synthesis of layered carbonitrides from biotic molecules for photoredox transformations. *Angew. Chem. Int. Ed. Engl.* **56**, 6627–6631 (2017).
44. Wang, Y., Yang, W., Chen, X., Wang, J. & Zhu, Y. Photocatalytic activity enhancement of core-shell structure g-C_3N_4@TiO_2 via controlled ultrathin g-C_3N_4 layer. *Appl. Catal. B Environ.* **220**, 337–347 (2018).
45. Boruah, P. K. & Das, M. R. Dual responsive magnetic Fe_3O_4–TiO_2/graphene nanocomposite as an artificial nanozyme for the colorimetric detection and photodegradation of pesticide in an aqueous medium. *J. Hazard Mater.* **385**, 121516 (2020).
46. Yuan, D. *et al.* Superparamagnetic polymer composite microspheres supported Schiff base palladium complex: an efficient and reusable catalyst for the Suzuki coupling reactions. *Chem. Eng. J.* **287**, 241–251 (2016).
47. Liu, Y. *et al.* One-pot hydrothermal synthesis of highly monodisperse water-dispersible hollow magnetic microspheres and construction of photonic crystals. *Chem. Eng. J.* **259**, 779–786 (2015).
48. Dong, Z., Wu, Y., Thirugnanam, N. & Li, G. Double Z-scheme ZnO/ZnS/g-C_3N_4 ternary structure for efficient photocatalytic H_2 production. *Appl. Surf. Sci.* **430**, 293–300 (2018).
49. Wang, D., Duan, H., Lü, J. & Lü, C. Fabrication of thermo-responsive polymer functionalized reduced graphene oxide@Fe_3O_4@Au magnetic nanocomposites for enhanced catalytic applications. *J. Mater. Chem. A* **5**, 5088–5097 (2017).
50. Zhang, H., Cao, D. & Bai, X. High rate performance of aqueous magnesium-ion batteries based on the δ-MnO_2@carbon molecular sieves composite as the cathode and nanowire VO_2 as the anode. *J. Power Sources* **444**, 227299 (2019).
51. Schuepfer, D. B. *et al.* Assessing the structural properties of graphitic and non-graphitic carbons by Raman spectroscopy. *Carbon* **161**, 359–372 (2020).
52. Tang, J. & Yamauchi, Y. MOF morphologies in control. *Nat. Chem.* **8**, 638–639 (2016).

Acknowledgments

This work is financially supported by National Natural Science Foundation of China (Grant No. 51503116), the Shandong Provincial Natural Science Foundation (Grant No. ZR2019BB063) and the Applied Basic Research Foundation of Qingdao City (Grant No. 19-6-2-13-cg).

Author contributions

M.M., Y.Y. and Y.C. wrote the main manuscript text. Y.Y. drew the flow chart and mechanism diagram. Y.M. ananlyzed the data. J.J.,Y.M., Z.W., W.H., S.W., M.L., D.M. and X.Y. collected data.All authors reviewed the manuscript.

Competing interests

The authors declare no competing interests.

Additional information

Correspondence and requests for materials should be addressed to Y.M.

Reprints and permissions information is available at www.nature.com/reprints.

Publisher's note Springer Nature remains neutral with regard to jurisdictional claims in published maps and institutional affiliations.